A High-Performance Piezoelectric Vibration Sensor

Bahareh Yaghootkar, Soheil Azimi, and Behraad Bahreyni, *Senior Member, IEEE*

***Abstract*— We are reporting on the design, fabrication, and characterization of wideband, piezoelectric vibration microsensors. Prototypes were fabricated in a commercial foundry process. The entire thickness of the handle wafer was employed to carve the proof-mass of the device, leading to high sensitivity at a reduced chip area. A thin layer of aluminum nitride was used for sensing the displacements of the proof-mass. A continuous membrane was employed for the device structure in order to push undesired modes to high frequencies. Sensors with different geometries were designed and fabricated. Analytic and finite element analyses were conducted to study device response. A lump element model was developed for the piezoelectric vibration sensor and used for the noise modeling of the complete sensor system. Various performance metrics for the devices were characterized experimentally. Fabricated prototypes exhibited sensitivities as high as 350 mV/g with first resonant frequencies of more than 10 kHz. These devices are particularly suited for emerging applications in high-frequency vibration sensing.**

***Index Terms*— Vibration sensor, piezoelectric, aluminum nitride, micro-electromechanical systems, noise model.**

I. INTRODUCTION

VIBRATION is a common phenomenon in daily lives. Unwanted vibrations can lead to accelerated aging and fatigue, and thus, can be detrimental to a wide variety of structures and machines. On the other hand, vibration pattern of structures is correlated to structural changes and can be used for preventive or early maintenance. Therefore, monitoring and detecting vibrations is critical for many systems and their surrounding environment. Various techniques have been developed so far for vibration detection. Laser Doppler Vibrometery, LDV, is an accurate and non-contact detection technique that works based on the Doppler-effect; sensing the frequency shift of reflected light from a moving surface [1]. Most vibration sensors, however, measure vibrations indirectly. Seismometers, for example, mostly measure velocity while many miniaturized vibration sensors measure acceleration. A geophone is another conventional tool for vibration measurements [2]. A geophone consists of a suspended proof-mass and a compliance mechanism where the movements of proof-mass due to external inertial forces are typically detected using electromagnetic or piezoelectric transducers. While accelerometers need to provide a response down to DC, vibration sensors are usually used for their ability to detect high-frequency inertial forces. Over the past two decades, microelectromechanical systems (MEMS) has been playing a profound role in the development of vibration sensors. Due to their small mass, MEMS accelerometers can achieve wide operating bandwidths, letting them in some cases to be used as vibration sensors. Various detection approaches have been developed for MEMS vibration sensors including piezoresistive, capacitive, tunneling, optical, and piezoelectric sensors. In case of optical sensing method the bulky optics for conditioning and controlling is the main drawback [3]. The small bandwidth and dynamic range are some disadvantages of tunneling approach. Piezoelectric transduction offers better linearity and long-term and temperature stability compared to piezoresistive and capacitive devices.

This work was supported by the Natural Sciences and Engineering Research Council of Canada.
Corresponding author: Behraad Bahreyni.
The authors are with the School of Mechatronic Systems Engineering, Simon Fraser University, Surrey, BC V3T 0A3, Canada (e-mail: behraad@ieee.org).

Digital Object Identifier 10.1109/JSEN.2017.2707063

A common piezoelectric material is lead zirconate titanate, PZT, owing to its high piezoelectric coefficients. A circular diaphragm piezoelectric accelerometer was reported by Wang et al, where they used PZT as the piezoelectric material of choice [4]. The outer and the inner electrodes were designed in such ways that they have the same area with an overall chip size of 6mm$\times$6mm. Multiple deposition and crystallization steps were conducted to achieve the desired 5.6μm PZT film thickness. The sensitivities ranged from 0.77$-$7.6pC/g (1g $\approx$ 9.8m.s^{-2}) with resonant frequencies from 3.7$-$35.3kHz. They attributed the sensor-to-sensor sensitivity variations to the silicon membrane thickness because of non-uniformity in the DRIE etching. The variation on membrane thickness was reported to be in the range of 6.1$-$44.4μm. Hindrichsen's et al reported a double ring circular piezoelectric accelerometer [5]. They used screen-printing technique to deposit a PZT film with a thickness of 24μm over the device membrane. The accelerometer has a charge sensitivity and voltage sensitivity of 0.23pC/g and 0.24mV/g as well as a first resonant frequency of 23.5kHz were reported for this sensor. A 480 μm-thick square shape proof-mass with an area of 2mm$\times$2mm was suspended with four beams, each having a thickness of 40 μm is reported by Beeby et al [6]. A 60μm thick layer of PZT was deposited using screen-printing technique was used as a piezoelectric sensing element. A sensitivity of 16pC/g along z-direction and a first resonant frequency of 7.55kHz were reported. However, the accelerometer exhibited a cross-axis sensitivity of 0.64pC/g.

Zinc oxide, ZnO, and aluminum nitride, AlN, are two alternative piezoelectric materials. A ZnO-based accelerometer was reported by Roger de Reus et al, where a seismic mass of 3mg was suspended by two 5μm thick beams [7]. They obtained a sensitivity of 0.1pC/g along z-direction and the calculated resonant frequency was 4.5kHz for a 1μm ZnO film. In recent years, the use of AlN as the piezoelectric layer in MEMS processes has been growing,

IEEE Proof

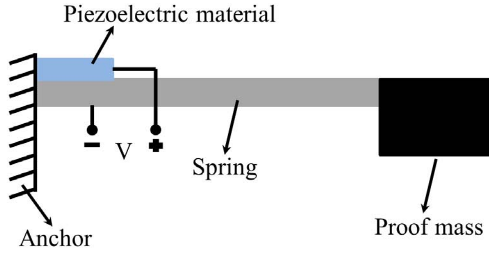

Fig. 1. Mass-spring model of piezoelectric-MEMS vibration sensor.

mainly due to its deposition process compatibility with other manufacturing steps. Although AlN's piezoelectric coefficient is about 10 times lower that PZT, its roughly 100 times lower dielectric constant results in a comparable or even higher figure of merit for energy harvesting and sensing [8], and hence AlN has been used widely for energy harvesting, power generation, and resonator application [9], [10]. AlN-based MEMS piezoelectric vibration sensors were designed and characterized by our group and the preliminary results have been reported [11].

There are emerging applications, such as localization of acoustic sources in infrastructure that require sensing vibrations in audio frequency range and beyond. The reset of the document describes our designs for high-frequency, sensitive piezoelectric MEMS vibration sensors. Devices were fabricated using PiezoMUMPS foundry process and were fully tested and characterized. A lump element model is presented for the piezoelectric vibration sensor and used for the noise modeling of the complete sensor system.

II. Sensor Model

A vibration sensor can be modeled as a mass-spring-damper system. Fig. 1 shows a schematic view of a typical piezoelectric MEMS vibration sensor where the springs are made from flexural beams. Various forms of damping are modeled as a damper with damping b (not shown in the figure). Newton's and Hooke's law imply:

$$F = Ma = K\Delta x \tag{1}$$

where M is the effective mass of proof-mass (Kg), Δx is its displacement (m), a is an external acceleration (m/s^2), and K is the effective spring constant of the structure (N/m) along the desired axis of sensitivity. For piezoelectric devices, the displacement leads to generation of electrical charge on electrodes. Piezoelectric element is typically deposited as a film on the flexural spring on areas near the proofmass or fixed support to maximize the device sensitivity. The piezoelectric effect is expressed mathematically through [12]:

$$D_i = \sum_J d_{iJ}\sigma_J + \sum_j \varepsilon_{ij} E_j \tag{2}$$

where D_i represents electrical displacement (C/m^2), d_{iJ} is the charge coefficient (C/N), σ_J is the applied stress (N/m^2), ε_{ij} is the permittivity (F/m), and E_j is the electric field (V/m). Indices $i, j = 1, 2, 3$ are the index components of the electric constituents E and D. Upper-case indices $I, J = 1, 2, 3, 4, 5, 6$ to index the reduced notation components of the mechanical stress, σ (values 4 to 6 for indices I and J correspond to shear stresses). The generated charge, q, can be calculated from:

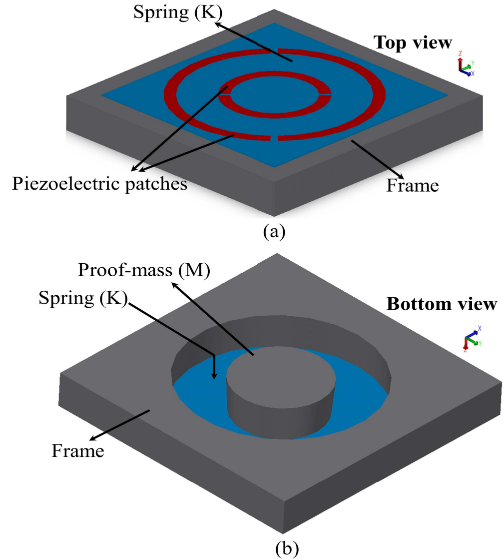

Fig. 2. 3-D schematic view of Piezoelectric-MEMS vibration sensor: (a) Top view of the device, (b) Bottom view of the device.

$$q = \int\int D_i dA_i \tag{3}$$

where A_i is the area of the electrodes. The charge q and the voltage generated across the sensor electrodes V are related through the capacitance of the sensor, C_s, as:

$$V = q/C_s \tag{4}$$

A. Design and Simulation of Piezoelectric Sensor

The proposed sensor structure is based on attaching a proof-mass to a membrane with piezoelectric transducers located at the places that are subject to the largest stresses with the movements of the proof-mass (see Fig. 2). The PiezoMUMPs foundry process, introduced in 2013, was used for the fabrication of three designs for the MEMS AlN piezoelectric vibration sensors [13]. The diameter of the proof-mass, thickness of the membrane and height of proof-mass for all designs are the same and equal to 1000μm, 10μm, and 400μm, respectively. The proof-mass is connected to the substrate through a continuous membrane. Two different membrane widths of 500μm and 200μm were considered for designs with a circular proof-mass (herein referred to as C_{500} and C_{200}, respectively). A third design with a square proof-mass with a side length of 1000μm and a membrane width of 200μm (referred to as S_{200}) was also laid out and fabricated alongside the other two devices. The overall die area for each sensor is 2.3mm$\times$2.3mm. Fig. 3 shows pictures of fabricated devices with different membrane geometries.

The structures were numerically analyzed based on finite element models in ANSYS. Figs. 4a and 4b show the stress analysis results for square and circular membrane respectively due to a 1g input acceleration. Figs. 5a and 5b illustrate the stress distribution along x-axis for these devices. Based on the

IEEE Proof

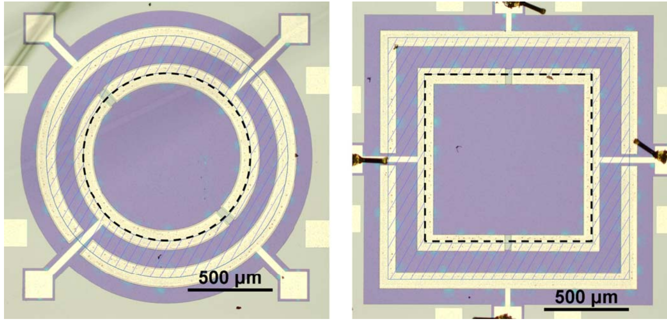

Fig. 3. Fabricated devices (C_{200} on the left and S_{200} on the right). The hashed area and dashed line correspond to the membrane area and boundary of the proof mass, respectively. The piezoelectric layer is only kept underneath the visible metal strips around the edges of the membrane.

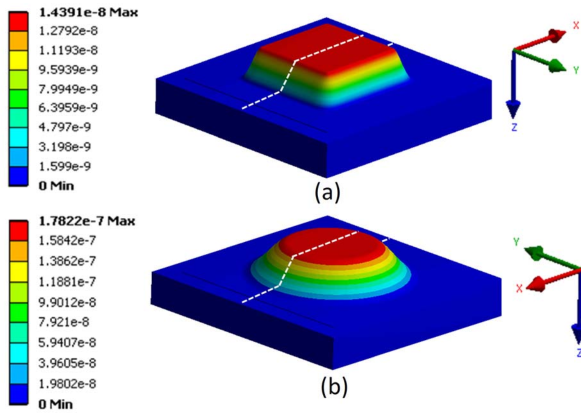

Fig. 4. Exaggerated membrane deformation due to 1 g input for square and circular membranes. (a) Square membrane with width of 200μm (S_{200}). (b) Circular membrane with width of 500μm (C_{500}).

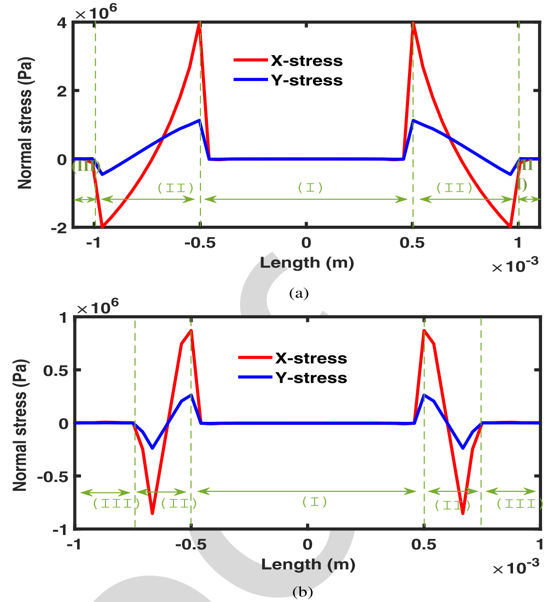

Fig. 5. X-stress and Y-stress analysis for square and circular shaped membrane along dashed line. (a) S_{xx} and S_{yy} for square membrane. (b) S_{xx} and S_{yy} for circular membrane. Regions (I), (II), and (III) represent proof mass, membrane, and anchors respectively.

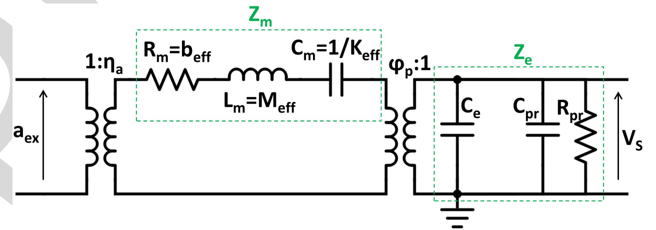

Fig. 6. Piezoelectric vibration sensor lumped element model.

stress analysis results, the AlN layer is deposited at the areas with highest stress.

Modal analysis on the structures indicated that the first mode for all devices is an out-of-plane piston mode. The first resonant frequency occurred at 14.4kHz, 41.9kHz, and 46.5kHz for sensors C_{500}, C_{200}, and S_{200}, respectively. The second mode, which was a dipole mode, occurred far away from the first resonant frequencies at 22.8kHz, 52.8kHz, and 60.9kHz for C_{500}, C_{200}, and S_{200} sensors, respectively.

B. Lumped Element Model

An electrical equivalent circuit was developed for the MEMS piezoelectric vibration sensor to assist in the interface circuit design. This equivalent circuit is also used to develop a noise model for the sensor system. In lumped element modeling, a transducer that is modeled as a mass-spring-damper system, using the force-voltage analogy between the mechanical and electrical domains, is represented by electrical components [14]. Ideal transformers are used for the conversion of energy between the electrical and mechanical.

Fig. 6 shows the equivalent circuit of the piezoelectric vibration sensor. The proof-mass-membrane structure is modeled as an inductance L_m which is equal to the total effective mass of the proof-mass and the membrane (M_{eff}), a capacitance C_m, the effective compliance of the structure ($1/K_{eff}$), and a resistance R_m which is equal to the total effective dissipation mechanisms (b_{eff}) including damping due to thermoelastic, viscous gas, and anchor losses. The excitation acceleration is converted into a mechanical force using the first transformer with a conversion ratio of $\eta_a = M_{eff}$. The piezoelectric coupling between mechanical and electrical domain is modeled using the combination of a transformer and a parallel capacitance in the electrical domain [15], [16]. The transformer turn ratio is:

$$\varphi_p = -d/C_m \tag{5}$$

where d is the effective piezoelectric charge constant. The electrical capacitance C_e represents the effective capacitance of the piezoelectric layer:

$$C_e = C_{ef}(1 - k^2) \tag{6}$$

where C_{ef} is the free capacitance of piezoelectric element:

$$C_{ef} = \varepsilon A_p/t_p \tag{7}$$

in which ε is the dielectric permittivity of the piezoelectric layer, A_P is the area of the piezoelectric ring and t_p is the thickness of the piezoelectric layer. k^2 is the impedance coupling factor and is defined as [16]:

$$k^2 = d^2/C_{ef}C_m \tag{8}$$

IEEE Proof

Using the equivalent circuit of Fig. 6, the overall open-circuit transfer function of the piezoelectric vibration sensor can be written as:

$$H_s\,(j\omega) = \frac{V_s}{a_{ex}} = \frac{\eta_a}{\varphi_p} \cdot \frac{Z_e}{Z_e + Z_m/\varphi_p^2} \tag{9}$$

where, Z_e and Z_m are the equivalent impedance of the electrical side and mechanical side respectively:

AQ:1

$$Z_e = \frac{R_{pr}}{1 + j\omega R_{pr}(C_e + C_{pr})} \tag{10}$$

and

$$Z_m = R_m + j\omega L_m + 1j\omega C_m \tag{11}$$

where R_{pr} is the parallel parasitic resistance of the piezoelectric layer caused by dielectric loss and C_{pr} is the parasitic capacitance of the bondpads and packaging.

III. Fabrication and Packaging

PiezoMUMPs offers a reliable fabrication process for piezoelectric MEMS devices by introducing a thin AlN piezoelectric film. The process begins with a 150mm n-type double-side polished Silicon-On-Insulator (SOI) wafer. The thicknesses of device layer, buried oxide layer, and handling layer were, 10μm, 1μm, 400μm, respectively. The sheet resistance of the device layer is in the range of 15-25Ω/sq. A 200nm oxide layer is grown thermally, and then patterned with 1st mask. It follows by deposition of 0.5μm piezoelectric AlN layer. A 2nd mask is used for patterning the piezoelectric layer. A metal layer is deposited and patterned using the 3rd mask to form the electrodes. The metal layer consists of 20nm chrome and 1μm aluminum. A 4th mask is used to from the structure. The device structure is patterned at the device layer of the SOI and etched using deep reactive ion etching (DRIE). At the last fabrication step, the handle layer is patterned using the 5th mask and etched by DRIE from the backside followed by removing the buried oxide layer using RIE. The fabrication process flow is shown in Fig. 7. Fabricated sensors were mounted in a ceramic Leadless Chip Carrier (LCC) package with spacers placed beneath the handle layer to create a gap between the proof-mass and package. The chip was then wirebonded for test and characterization.

IV. Experimental Results and Discussion

A. Modal Measurements

Initial dynamic testing of the vibration sensors was conducted using a Laser Doppler Vibrometer. Resonant frequency measurements were carried out using a Polytec MSA-050, which measures the velocity of vibrating structure. The sensor was actuated by applying a 100mV periodic chirp signal generated by the vibrometer system and applied to the piezoelectric patches. The first resonance modes are at 12.49kHz, 46.48kHz, and 42.81kHz for C_{500}, C_{200}, and S_{200}, respectively. Measurements were conducted to study the mode shapes of the devices at mode frequencies. In these experiments, the entire surface of the membrane was scanned using a controlled stage. The mode shapes for these resonant frequencies are presented in Fig. 8. These measurements confirmed that the

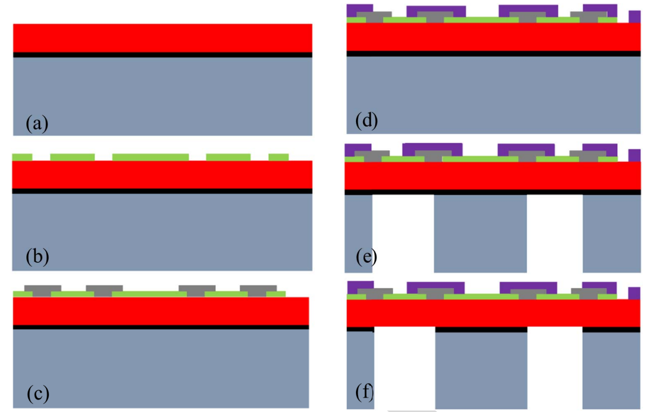

Fig. 7. PiezoMUMPS fabrication process steps: (a) silicon doping, (b) growth and patterning of oxide, 1st mask (c) AlN deposition and patterning, 2nd mask, (d) metal deposition and lift-off, 3rd mask (e) backside etching and patterning membrane 5th mask, (f) release.

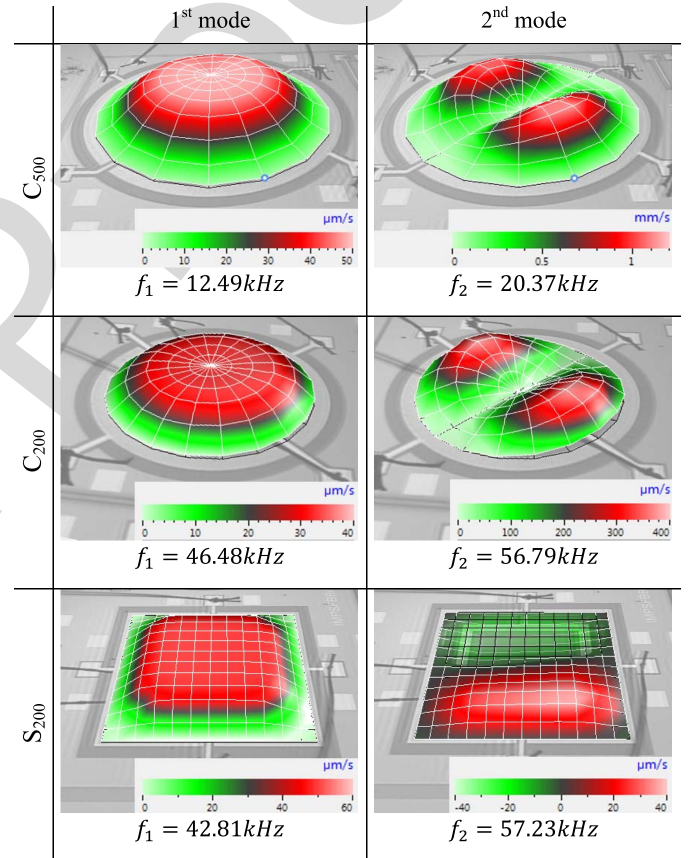

Fig. 8. Measured mode shapes for first and second resonance frequencies of sensors using scaning spot LDV.

first resonance mode is in fact the piston mode as expected. The second mode is a dipole-mode which occurred far from the first mode at 20.36kHz, 56.79kHz and 57.23kHz for C_{500}, C_{200}, and S_{200} devices, respectively.

B. Interface Electronics

The vibration sensor is a high-impedance device with a small output signal, requiring a signal conditioning circuit before being interfaced with a data acquisition system for

IEEE Proof

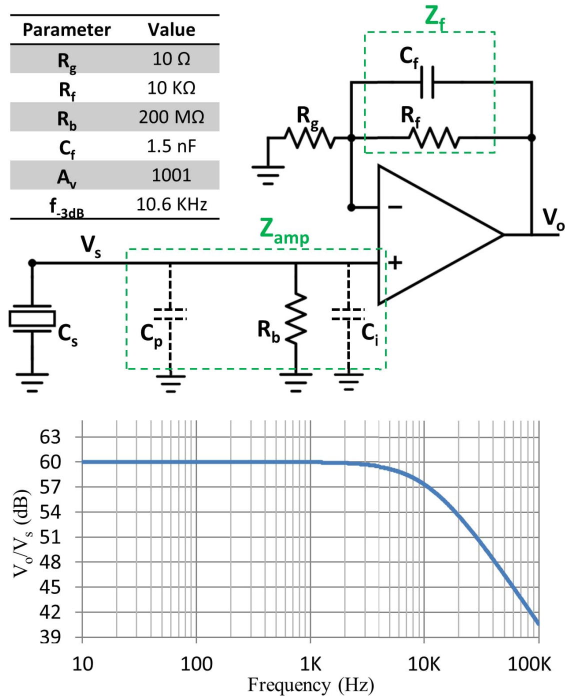

Fig. 9. The voltage amplifier interface circuit and its frequency response. Component values are shown in the inset table.

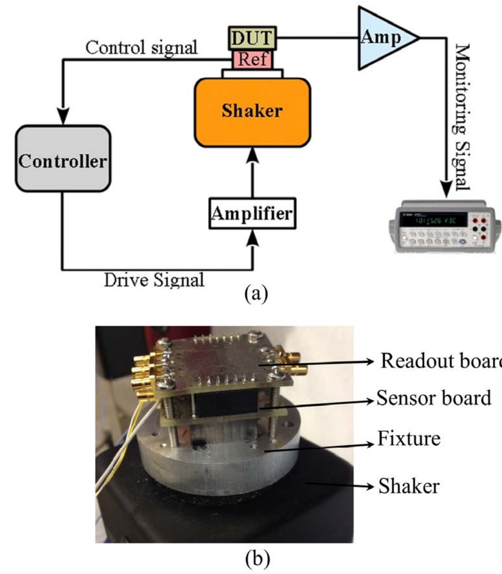

Fig. 10. Test setup. (a) Schematic of closed-loop vibration setup. (b) Readout circuit and sensor board are stacked and then mounted on the shaker.

characterization tests. There are two conventional topologies for interfacing piezoelectric transducers, namely charge amplifiers and voltage amplifiers. A charge amplifier holds a virtual ground across the transducer and converts the transducer's produced charge into voltage using a feedback capacitor. While the main advantage of the charge amplifier is that its gain is independent of parasitic capacitances parallel with the sensor, we found it unsuitable for these sensors. Our devices have small capacitances in range of tens of picofarads and in order to achieve a reasonable gain from a charge amplifier, a few picofarads feedback capacitor is required which is practically vulnerable to parasitic capacitances of the board and component packages. Therefore, a voltage amplifier topology was used as the interface circuit. Fig. 9 shows the schematic of this non-inverting voltage amplifier, where C_i is the input capacitance of the OpAmp and C_p is the line's parasitic capacitance. Bias resistor R_b provides a DC current path for the input stage of the amplifier while R_g and R_f set the flatband gain of the amplifier to $A_v = 1 + R_f/R_g$, and capacitor C_f forms a low-pass filter to set the upper cutoff frequency. Numerical values of these parameters and the simulated frequency response are provided in Fig. 10. A high input-impedance, voltage amplifier is needed to buffer and amplify the sensor's open-circuit output voltage. The LTC6240 OpAmp from Linear Technologies [17] is selected for its low noise current density, low input capacitance, and a proper gain-bandwidth product. The low input bias current of the OpAmp (0.2pA) ensures that the DC voltage imposed on the sensor by the R_b, is negligible ($\sim$40μV).

The transfer function of the voltage amplifier is:

$$H_{amp}(j\omega) = \frac{V_o}{V_s} = 1 + \frac{R_f}{R_g(1 + j\omega R_f C_f)} \tag{12}$$

Adding the voltage amplifier of Fig. 9 to the output of the sensor's equivalent circuit of Fig. 6 will generate a loading effect and hence changes the sensor's transfer function to

$$H_s'(j\omega) = \frac{\eta_a}{\varphi_p} \cdot \frac{Z_e'}{Z_e' + Z_m/\varphi_p^2} \tag{13}$$

where

$$Z_e' = Z_e || Z_{amp} = \frac{R_{pr}||R_b}{1 + j\omega(R_{pr}||R_b)(C_e + C_{pr} + C_p + C_i)} \tag{14}$$

As can be seen from equations (11) and (14), the amplifier's input capacitance reduces the voltage sensitivity of the system and thus it is important to use an amplifier with small input capacitance to address this issue. The overall transfer function of the system is

$$\begin{aligned} H_t(j\omega) &= H_s' \cdot H_{amp} \\ &= \frac{\eta_a}{\varphi_p} \cdot \frac{Z_e'}{Z_e' + Z_m/\varphi_p^2} \cdot \left[1 + \frac{R_f}{R_g\left(1 + j\omega R_f C_f\right)} \right] \end{aligned} \tag{15}$$

C. Sensitivity and Linearity

To evaluate the sensitivity and linearity of the vibration sensor, a dynamic test using a high-frequency shaker was carried out. A closed loop system consisting of the shaker, its controller, and a reference accelerometer was used for this purpose. The sensor was mounted on a printed circuit board and stacked on the electronics interface readout circuit board. The sensor board was then mounted on a fixture and fixed to the shaker. Fig. 10a illustrates the schematic of this setup. A picture of the actual test setup has been shown in Fig. 10b. The system was configured for a sine dwell test at an excitation frequency of 100Hz. The sensor was excited with acceleration magnitudes in the range of 200mg to 3g (i.e., the upper limit of the shaker at this frequency). The summary of each device specifications is collected in Table I.

TABLE I
DEVICE SPECIFICATIONS SUMMARY

Device Name	C_{500}	C_{200}	S_{200}
Membrane Width (μm)	500	200	200
Proof Mass Diameter (μm)	1000	1000	1000
1st Resonant Frequency (kHz)	14.4	41.9	46.5
2nd Resonant Frequency (kHz)	22.8	52.8	60.9
Piezoelectric-Element Capacitance (pF)	40	32	33
Total Sensitivity (mV/g)	355	176	162

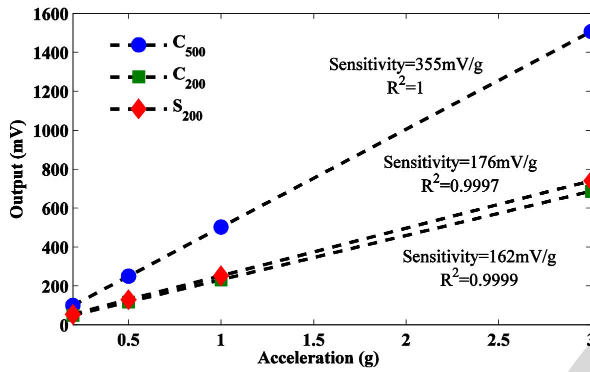

Fig. 11. Sensitivity and linearity results for C_{500}, C_{200}, and S_{200} sensors with the amplifier circuit.

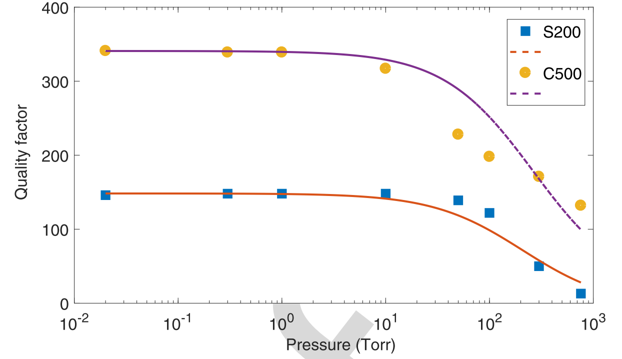

Fig. 12. Variation of Q-factor with pressure for the S_{200} and C_{500} devices (dashed lines are numerical fits).

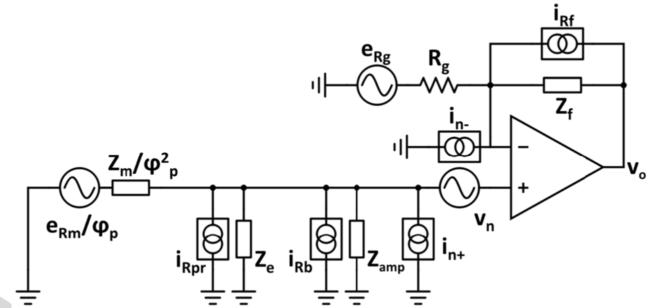

Fig. 13. Equivalent noise schematic of piezoelectric vibration sensor and amplifier.

The sensitivity and linearity results for the sensor-amplifier combination are shown in Fig. 11. As can be seen, the square shaped membrane has slightly higher sensitivity in comparison with the circular membrane with the same membrane width of 200μm. The open-circuit sensitivity (S_o) of each sensor is extracted from the total sensitivity (S) after considering the effect of the stray capacitances in equation (11) and (14):

$$S_o \approx \frac{S}{A_v} \cdot \frac{C_t}{C_e + C_{pr}} \tag{16}$$

where $C_t = C_e + C_{pr} + C_p + C_i$. The C_e values for each device can be found in Table I, C_{pr} and C_p are measured roughly 2pF and 3pF respectively where the value of C_i is taken from OpAmp's datasheet [17]. The open-circuit sensitivity of C_{500}, C_{200}, and S_{200} sensors are 440μV/g, 228μV/g, and 208μV/g, respectively.

Pressure-dependent damping characteristics of piezoelectric vibration sensors were evaluated using quality factor (Q-factor) measurements. Sensors were excited using an AC signal applied to one of the piezoelectric transducers while another piezoelectric transducer was used for the detection of induced displacements. The variation of Q-factor under various pressures was then studied. The Q-factor for C_{500} was ∼340 for pressures below 1Torr and dropped to 132 at atmospheric pressure. For device S_{200}, a dramatic 10-fold change in Q-factor was observed as the pressure changed from ∼ 100Torr to atmosphere. Pressure dependence of quality factor of sensors has been shown on Fig. 12. Based on the data, it can be deduced that at pressures below 10Torr, other loss mechanisms will start to dominate the total losses for both devices.

D. Noise Measurement

The lumped element model from section II-B is combined with the amplifier circuitry to develop a noise model for the vibration sensor. The noise model circuit with all noise sources is shown in Fig. 13. The total noise of the system e_{ntot} consists of two noise sources: the piezoelectric sensor's thermal noise e_{ns} and the amplifier's noise e_{na}. The noise of the piezoelectric sensor has two components, the mechanical-thermal noise e_{nsm} which is determined by the mechanical resistance noise of the damped oscillating proof-mass and the electrical-thermal noise e_{nse} which is determined by the electrical loss in the piezoelectric layer [18], [19].

The total noise power spectral density can be calculated by the superposition of all noise powers if the sources are assumed uncorrelated:

$$\overline{e_{ns}^2} = \overline{e_{nsm}^2} + \overline{e_{nse}^2} \tag{17}$$

and

$$\overline{e_{ntot}^2} = A_n^2 \overline{e_{ns}^2} + \overline{e_{na}^2} \tag{18}$$

where $A_n = 1 + Z_f/R_g$ is the noise gain of the amplifier. In the low frequency and flatband region where the frequency is well below the f_{-3dB}, knowing that R_{pr}(≈14GΩ) ≫ R_b ≫

TABLE II
PERFORMANCE COMPARISON OF THE PRESENTED SENSOR WITH OTHER VIBRATION SENSORS

Reference	Transduction	Die Area (mm×mm)	First Resonant Frequency (kHz)	Sensitivity (mV/g)	Total Noise @ 1kHz (μg/√Hz)
This work (C_{500})	Piezoelectric (AlN)	2.3×2.3	12.5	355	200
This work (S_{200})	Piezoelectric (AlN)	2.3×2.3	42.8	176	200
Gerfers et al. 2007 [21]	Piezoelectric (AlN)	6.8×6.8	1.1	400	0.67
Hindrichsen et al. 2009 [5]	Piezoelectric (PZT)	10×10	23.5	0.24	–
Wang et al. 2002 [4]	Piezoelectric (PZT)	6×6	17.4	14	–
Vogl et al. 2009 [22]	Piezoresistive	3.5×3.5	10.3	0.19	7000
Liu et al. 2013 [23]	Piezoresistive	5×5	13.3	0.545	0.03
Speller et al. 2004 [24]	Capacitive	6.5×5	6	–	0.05
Roy et al. 2014 [25]	Piezoresistive	3.5×3.5	1.5	4	–

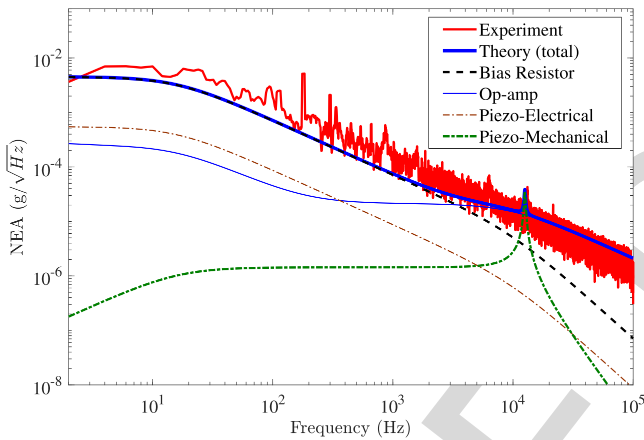

Fig. 14. Experimental and theoretical spectral densities for noise equivalent acceleration for sensor C_{500}.

$R_f \gg R_g$, the total noise spectral density is:

$$\overline{e_{ntot}^2} \approx \left(\frac{R_f}{R_g}\right)^2 \left(\frac{4K_B T R_b + R_b^2 \overline{i_n^2}}{1+(\omega R_b C_t)^2} + v_n^2\right) \quad (19)$$

where K_B is the Boltzmann's constant, and i_n and v_n are the amplifier's input noise current and voltage density, respectively. Fig. 14 shows the noise equivalent acceleration (NEA) at the amplifier's output for each noise source for the sensor C_{500}. As can be seen, the dominant noise sources are the thermal noise of the bias resistor and the input current and voltage noises of the op-amp at higher frequencies [17]. The sensor's electrical-thermal noise is dominated by the bias resistor's thermal noise while the mechanical-thermal noise of the sensor [18] ($\sqrt{4K_B T \omega_0 / mQ} \approx 1\mu g/\sqrt{Hz}$) is negligible comparing to the other noise sources in the operation bandwidth. In order to verify the theoretical noise model, the sensor system's overall noise spectral density was measured with a 24-bit, 204.8kS/s dynamic signal analyzer (NI PXI-4462) and the algorithm described in [20]. As can be seen in Fig. 16 the experimental and theoretical noise floors are in good agreement. Performance of the vibration sensor is compared to other MEMS vibration sensors in Table II [21]–[25]. Note that the noise performance of the sensors reported here were limited by the common interface electronics used for both sensors.

V. CONCLUSIONS

The design, fabrication, analysis, and characterization of vibration microsensors fabricated in a standard MEMS foundry process were discussed. The devices employed an AlN layer for piezoelectric transduction of a proof-mass to electric charge which was measured with a simple interface circuit. The proof-mass of the devices was carved from the entire thickness of the handle wafer. This allows the devices to attain a high sensitivity while occupying a relatively small chip area. Using a continuous membrane for device compliance, a wide operating bandwidth was achieved. The noise performance of the developed sensors was limited by the interface electronics, where the inherent micro-mechanical noise of the device ($\sim 1\mu g/\sqrt{Hz}$) was buried in electronic noise ($\sim 200\mu g/\sqrt{Hz}$), leaving room for significant noise performance improvement by further research on interface electronics. The high sensitivity, operating bandwidth, and low inherent noise of these sensors enables their use in many existing and emerging applications of vibration sensors.

ACKNOWLEDGMENTS

The authors would like to thank CMC Microsystems for providing access to the foundry services and numerical simulation tools. We also thank Oldooz Pooyanfar for assistance with chip layout.

REFERENCES

[1] H. H. Nassif, M. Gindy, and J. Davis, "Comparison of laser Doppler vibrometer with contact sensors for monitoring bridge deflection and vibration," *NDT E Int.*, vol. 38, no. 3, pp. 213–218, Apr. 2005.
[2] J. Bernstein, R. Miller, W. Kelley, and P. Ward, "Low-noise MEMS vibration sensor for geophysical applications," *J. Microelectromech. Syst.*, vol. 8, no. 4, pp. 433–438, Dec. 1999.

IEEE Proof

[3] S. Kon and R. Horowitz, "A high-resolution MEMS piezoelectric strain sensor for structural vibration detection," *IEEE Sensors J.*, vol. 8, no. 12, pp. 2027–2035, Dec. 2008.

[4] L. P. Wang, K. Deng, L. Zou, R. Wolf, R. J. Davis, and S. Trolier-McKinstry, "Microelectromechanical systems (MEMS) accelerometers using lead zirconate titanate thick films," *IEEE Electron Device Lett.*, vol. 23, no. 4, pp. 182–184, Apr. 2002.

[5] C. C. Hindrichsen, J. Larsen, E. V. Thomsen, K. Hansen, and R. Lou-Møller, "Circular piezoelectric accelerometer for high band width application," in *Proc. IEEE Sensors*, Oct. 2009, pp. 475–478.

[6] S. P. Beeby, J. N. Ross, and N. M. White, "Design and fabrication of a micromachined silicon accelerometer with thick-film printed PZT sensors," *J. Micromech. Microeng.*, vol. 10, no. 3, pp. 322–328, 2000.

[7] R. de Reus, J. O. Gulløv, and P. R. Scheeper, "Fabrication and characterization of a piezoelectric accelerometer," *J. Micromech. Microeng.*, vol. 9, no. 2, pp. 123–126, 1999.

[8] M. Tilli, T. Motooka, V.-M. Airaksinen, S. Franssila, M. Paulasto-Krockel, and V. Lindroos, *Handbook of Silicon Based MEMS Materials and Technologies*. William Andrew, 2015.

[9] A. Heidari, Y.-J. Yoon, M. I. Lee, L. Khine, M. K. Park, and J. M. L. Tsai, "A novel checker-patterned AlN MEMS resonator as gravimetric sensor," *Sens. Actuators A, Phys.*, vol. 189, pp. 298–306, Jan. 2013.

[10] R. Abdolvand, B. Bahreyni, J. E.-Y. Lee, and F. Nabki, "Micromachined resonators: A review," *Micromachines*, vol. 7, no. 9, p. 160, Sep. 2016.

[11] B. Yaghootkar, S. Azimi, and B. Bahreyni, "Wideband piezoelectric MEMS vibration sensor," in *Proc. IEEE SENSORS*, Nov. 2016, pp. 1–3.

[12] S. D. Senturia, *Microsystem Design*. Boston, MA, USA: Kluwer Academic Publishers, 2000.

[13] A. Cowen, G. Hames, K. Glukh, and B. Hardy, "PiezoMUMPsTM design handbook, rev 1.3," MEMSCAP Inc., Tech. Rep., 2014.

[14] H. A. C. Tilmans, "Equivalent circuit representation of electromechanical transducers: I. Lumped-parameter systems," *J. Micromech. Microeng.*, vol. 6, no. 1, p. 157, Mar. 1996.

[15] H. A. C. Tilmans, "Equivalent circuit representation of electromechanical transducers: II. Distributed-parameter systems," *J. Micromech. Microeng.*, vol. 7, no. 4, p. 285, 1997.

[16] S. A. N. Prasad *et al.*, "Analytical electroacoustic model of a piezoelectric composite circular plate," *AIAA J.*, vol. 44, no. 10, pp. 2311–2318, 2006.

[17] *LTC6240—Single 18 MHz, Low Noise, Rail-to-Rail Output, CMOS Op Amp—Linear Technology*, accessed on Feb. 28, 2017. [Online]. Available: http://www.linear.com/product/LTC6240

[18] T. B. Gabrielson, "Mechanical-thermal noise in micromachined acoustic and vibration sensors," *IEEE Trans. Electron Devices*, vol. 40, no. 5, pp. 903–909, May 1993.

[19] F. A. Levinzon, "Noise of piezoelectric accelerometer with integral FET amplifier," *IEEE Sensors J.*, vol. 5, no. 6, pp. 1235–1242, Dec. 2005.

[20] S. Moghaddam, "Noise measurement in microsensor applications," M.S. thesis, School Mech. Syst. Eng., Simon Fraser Univ., Burnaby, BC, Canada, 2016.

[21] F. Gerfers, M. Kohlstadt, H. Bar, M. Y. He, Y. Manoli, and L. P. Wang, "Sub-μg ultra-low-noise MEMS accelerometers based on CMOS-compatible piezoelectric AlN thin films," in *Proc. Int. Solid-State Sens., Actuators Microsyst. Conf. (TRANSDUCERS)*, Jun. 2007, pp. 1191–1194.

[22] A. Vogl *et al.*, "Design, process and characterisation of a high-performance vibration sensor for wireless condition monitoring," *Sens. Actuators A, Phys.*, vol. 153, no. 2, pp. 155–161, Aug. 2009.

[23] Y. Liu, Y. Zhao, W. Wang, L. Sun, and Z. Jiang, "A high-performance multi-beam microaccelerometer for vibration monitoring in intelligent manufacturing equipment," *Sens. Actuators A, Phys.*, vol. 189, pp. 8–16, Jan. 2013.

[24] K. E. Speller and D. Yu, "A low-noise MEMS accelerometer for unattended ground sensor applications," *Proc. SPIE*, vol. 5417, pp. 63–72, Sep. 2014.

[25] A. L. Roy, H. Sarkar, A. Dutta, and T. K. Bhattacharyya, "A high precision SOI MEMS–CMOS ±4g piezoresistive accelerometer," *Sens. Actuators A, Phys.*, vol. 210, pp. 77–85, Apr. 2014.

Bahareh Yaghootkar received the B.Sc. degree from Azad University, Iran, in 2003, the M.Sc. degree from the University of Technology, Malaysia, in 2009, and the Ph.D. degree from Concordia University, Canada, in 2014, respectively, all in electrical and electronics engineering. In 2009, she was a Research Engineer with the National University of Singapore in the field of BioMEMs. In 2015, she joined the IMuTS Laboratory, Simon Fraser University, where she is currently a Post-Doctoral Fellow on fabrication and characterization of MEMS sensors. Her research areas include fabrication and characterization of nanostructures and MEMS devices.

Soheil Azimi received the B.S. degree from the University of Tehran, Tehran, Iran, in 2005, the M.S. degree from the Sharif University of Technology, Tehran, Iran, in 2007, and the Ph.D. degree from the University of Tehran, Tehran, Iran, in 2012, all in electrical engineering. From 2012 to 2015, he was a Research Fellow at the University of Tehran, where he worked on hardware/software development for automated semiconductor equipment. In 2015, he joined Simon Fraser University, BC, Canada as a Post-Doctoral Research Fellow. His research interests include design and fabrication of microsensors and microactuators, their mixed-signal interface electronics, and Internet of Things applications of microsensors

Behraad Bahreyni (S'98–M'07–SM'14) received the B.Sc. degree in electronics engineering from the Sharif University of Technology, Iran, in 1999, and the M.Sc. and Ph.D. degrees in electrical engineering from the University of Manitoba, Canada, in 2001 and 2006, respectively. He is an Associate Professor and the Founding Director of the IMuTS Laboratory, Simon Fraser University, BC, Canada. He was a Post-Doctoral Researcher with the NanoSicence Center, Cambridge University, U.K., where he conducted research on interface circuit design for microresonators. He joined Simon Fraser University in 2008 after one-year tenure in industry as a MEMS design engineer. In 2016, he was with NXP Semiconductors, The Netherlands, conducting research on advanced signal processing methods for sensing applications. Over the past decade, his research activities have focused on the design and fabrication of micro/nano-sensors, their interface electronics, and the required signal processing algorithms. He is the author of about 100 technical publications including a book on the fabrication and design of resonant micro devices

IEEE Proof

AUTHOR QUERIES

AUTHOR PLEASE ANSWER ALL QUERIES

PLEASE NOTE: We cannot accept new source files as corrections for your paper. If possible, please annotate the PDF proof we have sent you with your corrections and upload it via the Author Gateway. Alternatively, you may send us your corrections in list format. You may also upload revised graphics via the Author Gateway.

AQ:1 = Equation (10) and (11) is present twice in the manuscript, so we have renumbered the other equations and their citations accordingly. Please confirm.
AQ:2 = Please provide the in-text citation and the corresponding image for Fig. 15.
AQ:3 = Please provide the corresponding image for Fig.16.
AQ:4 = Please provide the publisher location for ref. [8].
AQ:5 = Please confirm the author names and title for ref. [13]. Also provide the organization location and report no.
AQ:6 = Please confirm the volume no. for ref. [24].

IEEE Proof